Michigan Technological University

Michigan Technological University
Digital Commons @ Michigan Tech

Dissertations, Master's Theses and Master's Reports

2023

AN EXPERIMENTALLY VALIDATED COMPUTATIONAL MODEL FOR THE DEGRADATION AND FRACTURE OF MAGNESIUM-BASED IMPLANTS IN A CHEMICALLY CORROSIVE ENVIRONMENT

Mark M. Ousdigian
Michigan Technological University, mmousdig@mtu.edu

Copyright 2023 Mark M. Ousdigian

Recommended Citation

Ousdigian, Mark M., "AN EXPERIMENTALLY VALIDATED COMPUTATIONAL MODEL FOR THE DEGRADATION AND FRACTURE OF MAGNESIUM-BASED IMPLANTS IN A CHEMICALLY CORROSIVE ENVIRONMENT", Open Access Master's Thesis, Michigan Technological University, 2023.
https://doi.org/10.37099/mtu.dc.etdr/1579

Follow this and additional works at: https://digitalcommons.mtu.edu/etdr

 Part of the Biomaterials Commons, and the Computer-Aided Engineering and Design Commons

AN EXPERIMENTALLY VALIDATED COMPUTATIONAL MODEL FOR THE DEGRADATION AND FRACTURE OF MAGNESIUM-BASED IMPLANTS IN A CHEMICALLY CORROSIVE ENVIRONMENT

By

Mark M. Ousdigian

A THESIS

Submitted in partial fulfillment of the requirements for the degree of

MASTER OF SCIENCE

In Mechanical Engineering

MICHIGAN TECHNOLOGICAL UNIVERSITY

2023

© 2023 Mark M. Ousdigian

This thesis has been approved in partial fulfillment of the requirements for the Degree of MASTER OF SCIENCE in Mechanical Engineering.

Department of Mechanical Engineering - Engineering Mechanics

Thesis Advisor: *Dr. Trisha Sain*

Committee Member: *Dr. Paul Sanders*

Committee Member: *Dr. Roger Guillory II*

Department Chair: *Jason R. Blough*

Dedication

To my mom and dad,

who taught me the value of hard work. Your love and support have been instrumental in my academic journey, and I would not be where I am today without you.

Contents

List of Figures

List of Tables

Acknowledgments

First and foremost, I would like to express my sincere gratitude to my advisor, Dr. Trisha Sain, for providing me with the opportunity to conduct this research and for her support and guidance throughout the project. She has pushed me to do my best work while also demonstrating patience, and I am grateful for her mentorship.

Next I would like to thank my committee members Dr. Paul Sanders and Dr. Roger Guillory II. In addition to serving on my committee, they both provided invaluable insights throughout my research. I am deeply grateful for their expertise, and the resources they made available to me.

I would also like to thank Tom Wood, Paul Fraley, and Dan Seguin for their support and assistance throughout the experimental phase of my project. Their availability and willingness to help with any issues that arose were crucial to the success of my research, and I am fortunate to have had their help.

Lastly, I would like to than the Portage Health Foundation for its financial support of my research.

Abstract

In the orthopedic and cardiovascular fields there is a growing interest for biodegradable implants, which can be naturally degraded in the body environment over time so that no extraction surgery is required. These implants must be designed to maintain their strength until the fracture has healed in the body, which could be influenced by many factors such as -the patient's age, activities, body weight, pre-existing conditions etc. Hence, an ideal implant design should be done on a patient-by-patient basis. In the present work, a computational model is developed to predict the degradation and fracture of magnesium-based implants in a stress-coupled chemically corrosive environment to better predict their lifespan. The degradation is modeled as a diffusion-driven dissolution of magnesium from the implant into the surrounding fluid simulating the body environment, and as the concentration of magnesium decreases in the implant, its mechanical integrity weakens. A phase-field fracture model is also implemented to predict the initiation and growth of cracks in the specimen. To validate the model, experiments are conducted by exposing pure magnesium specimens to an artificial body solution for various durations of time and subsequently tensile testing them. The model is numerically implemented in finite elements and the parameters are calibrated from experiments to successfully predict the fracture/degradation response of the Mg-implants under mechanical loads.

Chapter 1

Introduction

1.1 Introduction

Due to their bio-friendly properties, Mg based implants are gaining attention in various biomedical applications such as orthopedics and the cardiovascular field [1, 2, 3]. Implants fabricated using Mg and its alloys for orthopedics help to reduce the stress shielding effect due to the similarity of the stiffness between natural bone and Mg [3, 4, 5]. Additionally, Mg is an essential element to the body, so as the implants degrade the Mg is absorbed by the body. Recent literature has even indicated Mg based implants promote bone growth in the surrounding area [6, 7, 8, 9]. However, the uncontrolled degradation of Mg based implants in the physiological environment

still poses a challenge in long-term stability of these implants. One particular issue that Mg based implants face is Stress Corrosion Cracking (SCC), which is caused by hydrogen embrittlement during the degradation process [10, 11, 12]. For this reason, researchers are looking for ways to estimate the effects of corrosion, so that the implant life can be more easily predicted.

The mechanistic understanding of Mg degradation in aqueous solutions has been well reported through experimental approaches over the years. Several studies found that the purity of pure magnesium had a major impact on it's corrosion rate. Firstly, Han et all [13] reported that pure Mg of 99.98 wt percent had trace impurities of Fe (0.0014 wt %) which led to preferred crystallographic pitting (PCP) and correspondingly high corrosion rates. They found that the addition of Mn (up to 0.51 wt %) to their samples created a compound with the Fe which significantly reduced the PCP in their samples. Song [14] found that high purity Mg (HP-Mg: 0.0045 wt% Fe, <0.002 wt%Cu and <0.002 wt% Ni) had the lowest corrosion rate amongst several Mg alloys in Hank's Balanced Salt Solution (HBSS). Shi et al [15] reported that a Mg-5Zn alloy made with ultra-high-purity (UP) Mg actually had a higher corrosion rate than UP Mg on its own, although Hofstetter et al. [16] found that a Mg–Zn–Ca alloy had an even lower corrosion rate than the UP Mg.

Many studies have also explored the effect of grain size on the corrosion rate of Mg. Some found that smaller grains resulted in higher corrosion rates [9, 17], while the majority found that smaller grains resulted in lower corrosion rates due to the formation

of a dense magnesium hydroxide layer that protects the sample surface [13, 18, 19, 20]. It is worth noting that studies have been done exploring the corrosion rate of Mg both *in vivo* and *in vitro*, and results indicate *in vitro* experiments have higher corrosion rates by 1-4x [21, 22]. Bowen, Drelich, and Goldman also reported that mechanical responses such as tensile strength and strain to failure had multipliers of 2.2 and 3.1x for *in-vitro* vs *in vivo* [23].

Combining the experimental insights with computational modeling can provide better understanding of the degradation behavior as corrosion testing of Mg implants can be time consuming and costly. There are number of studies concerning the modeling and simulation of Mg based metal corrosion. For example, continuum damage mechanics based modeling [24] to determine the mechanical integrity of the Mg based implants and the modeling approaches based on the mass transport of the ions to incorporate the diffusion-reaction process, were reported [25, 26]. Another application of the computational modeling of the biodegradation process was the prediction of how biodegradation affects the shape of the medical device or implant over time. For this purpose, the use of level set method (LSM) has been used to track the moving corrosion interfaces and study the effect of degradation on the mechanical properties of the implant across the moving interface [27].In summary, the existing computational approaches are limited in predicting the response of the Mg-implants during a coupled mechanical deformation in a corrosive environment.

Chapter 2

A large deformation elasto-plastic phase-field fracture constitutive model for pure Mg

In this chapter we describe the large deformation elasto-plastic constitutive model coupled with phase-field fracture for capturing the rate dependent mechanical response of pure-Mg.

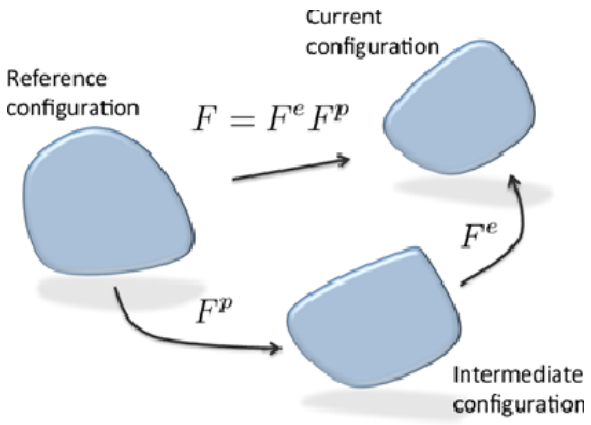

Figure 2.1: Schematic showing the multiplicative decomposition of the deformation gradient in large deformation elasto-plastic constitutive framework.

2.1 Elasto-plastic constitutive model

Following the large deformation theory of metal plasticity, we based our theory on the Kroner decomposition of the deformation gradient as (Fig. 2.1),

$$\mathbf{F} = \mathbf{F}^e\mathbf{F}^p \tag{2.1}$$

where the deformation gradient $\mathbf{F}$ is defined over a smooth one-to-one mapping between the reference configuration $\mathbf{X}$ and the current configuration as, $\mathbf{x} = \chi(\mathbf{X}, t)$ with $\mathbf{F} = \nabla\chi$. As is standard in continuum mechanics we assume, $J = det(\mathbf{F}) > 0$ and $J^e = det(\mathbf{F}^e) > 0$; We also assume that the plastic flow to be isochoric, i.e.,

$$det\mathbf{F}^p = 1 \quad \Rightarrow \quad J = J^e = det\mathbf{F}^e \tag{2.2}$$

In Eqn.2.1 $\mathbf{F}^e$ represents the local deformation of the Mg crystal due to stretch and rotation of the microscopic structure; and $\mathbf{F}^p$ represents the local inelastic deformation due to motion of the dislocations. The evolution equation for $\mathbf{F}^p$ is given by,

$$\dot{\mathbf{F}}^p = \mathbf{D}^p \mathbf{F}^p \tag{2.3}$$

In the present work an associative flow rule based on J_2 flow theory with isotropic hardening has been considered to describe the plastic strain evolution. Based on the standard J_2 plasticity the flow rule for the plastic strain is given by,

$$\mathbf{D}^p = \sqrt{\frac{1}{2}} \nu^p \mathbf{N}^p \tag{2.4}$$

where ν^p is the equivalent plastic shear strain rate as given by,

$$\nu^p = \nu_0 \left(\frac{\bar{\tau}}{\sigma_y} \right)^{1/m} \tag{2.5}$$

In Eqn.2.5 a power law type model is chosen for the plastic shear strain rate evolution with exponent m and reference shear strain rate ν_0. Both of these coefficients can be determined from the rate dependent experimental stress-strain data. A high value of m corresponds to the rate-insensitive limit. Further $\bar{\tau}$ represents the effective

deviatoric component of the elastic Mandel stress measure as given by,

$$\bar{\tau} = \sqrt{\frac{1}{2}\mathbf{M}_0^e : \mathbf{M}_0^e} \tag{2.6}$$

with $\mathbf{M}_0^e$ representing the elastic, deviatoric component of the Mandel stress as,

$$\mathbf{M}^e = 2G\mathbf{E}^e + \lambda(tr\mathbf{E}^e)\mathbf{I} \tag{2.7}$$

and the deviatoric component is $\mathbf{M}_0^e = \mathbf{M}^e - \frac{1}{3}tr(\mathbf{M}^e)\mathbf{I}$; in Eqn.2.7 G is the shear modulus and $\lambda = K - (2/3)G$ the Lame parameter, and K is the bulk modulus. It is important to note that the strain measure used here is the logarithmic Hencky strain calculated as, $\mathbf{E}^e = ln(\mathbf{U}^e)$, where $\mathbf{U}^e$ is the elastic stretch calculated using the standard polar decomposition of $\mathbf{F}^e = \mathbf{R}^e\mathbf{U}^e$.

In Eqn. 2.4, $\mathbf{N}^p$ represents the direction of the plastic flow, as given by

$$\mathbf{N}^p = \frac{\mathbf{M}_0^e}{\sqrt{2}\bar{\tau}} \tag{2.8}$$

for an associative flow behavior. In Eqn.2.5 σ_y represents the current yield strength responsible for the deformation resistance of pure Mg. Assuming an isotropic hardening behavior, the evolution for σ_y is considered as,

$$\dot{\sigma}_y = h(\sigma_{y,s} - \sigma_y)\nu^p \tag{2.9}$$

where h is the hardening modulus and $\sigma_{y,s}$ is the saturation yield strength. Finally, the Cauchy stress is related to the Mandel stress as,

$$\mathbf{T} = J^{-1}\mathbf{R}^e\mathbf{M}^e\mathbf{R}^e \tag{2.10}$$

2.2 Phase-field fracture model for ductile materials

Fracture is one of the most common sources of failure in engineering structures, and much work is still being done on modeling it because it is a complicated phenomena. In the last decade or so, the phase-field fracture method has emerged as a promising tool for modeling fracture. Rather than modeling a sharp crack, phase-field models create a diffuse crack that transitions from the intact to the fully broken material. This method is able to predict the initiation and propagation of cracks, including branching and merging, without a predefined crack path or changes to the original mesh.

Initially phase-field formulations were predominantly focused on fracture in brittle materials [28]. More recently, the approach has been extended to ductile materials by incorporating plastic strains in the phase-field crack evolution [29, 30]. In the present work, a recent theory proposed by Borden et al.[31] is used for modeling phase-field

fracture in ductile materials, which incorporates a degraded yield function and plastic softening beyond yielding.

The following section describes the fundamental equations related to the variational theory of fracture as outlined by Borden et al.[31]. Using Griffith's theory of brittle fracture, the stored energy of a fractured body can be written as,

$$\Psi(\mathbf{F}, \Gamma_0) = \int_{\Omega_0} W(\mathbf{F}) d\Omega_0 + \int_{\Gamma_0} G_c d\Gamma_0 \tag{2.11}$$

where W is the elastic strain energy density (per unit volume) in the reference configuration and G_c is the critical fracture energy per unit crack area, dissipated over the crack surface Γ_0. Bourdin et al. [32] then introduced a regularized phase-field approximation of a sharp, discrete crack (Fig 2.2)-following which Eqn. 2.11 takes the form,

$$\bar{\Psi}(\mathbf{F}, d, \nabla d) = \int_{g(d)\Omega_0} W(\mathbf{F}) d\Omega_0 + \int_{\Omega_0} G_c \Gamma_d(d, \nabla d) d\Omega_0 \tag{2.12}$$

where $d \in [0, 1]$ is the phase-field parameter, $g(d)$ is the degradation function that acts to reduce the elastic strength of the material, and

$$\int_{\Omega_0} G_c \Gamma_d(d, \nabla d) d\Omega_0 \approx \int_{\Gamma_0} G_c d\Gamma_0 \tag{2.13}$$

is the volumetric approximation of the energy contribution from the crack surface. The function Γ_d is called the crack density functional, which typically takes the form

[33]

$$\Gamma_d = \frac{1}{2l_c}[d^2 + l_c^2|\nabla d|^2] \tag{2.14}$$

where l_c is a length scale parameter that determines the width of the phase-field crack (Fig2.2). As proven in the phase-field literature $l_c \to 0$ satisfies the so called $\Gamma-$ convergence criteria for representing a sharp crack geometry [33]. This condition provides certain constrain to choose the length scale parameter for the regularized crack description. In Eqn. 2.14, the 2nd term involves the gradient of phase-field variable d, which is introduced to add the non-local nature of the damage evolution. The addition of the non-local ∇d term renders the mesh-objectivity of the phase-field fracture method, which is a persistent issue in other continuum damage mechanics models.

For the energy functional presented in Eqn. 2.12 crack growth is driven by elastic

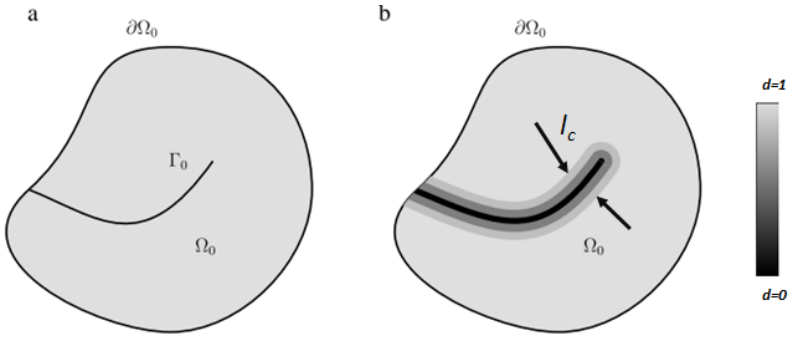

Figure 2.2: The diffuse crack approximation of a sharp crack in phase-field fracture theory [31].

strain energy. To extend this theory for ductile materials such as pure Mg, where plastic deformation is dominant, a mechanism is considered to incorporate plastic

yielding to contribute to crack growth. Hence, based on the approach [31], the stored energy functional has been modified to add an effective plastic work contribution W_p as,

$$\bar{\Psi}(\mathbf{F}, d, \nabla d, \mathbf{F}^p, \alpha) = \int_{\Omega_0} \left[g(d) W(\mathbf{F}, \mathbf{F}^p) + g_p(d) W_p(\alpha) \right] d\Omega_0 + \int_{\Omega_0} G_c \Gamma_d(d, \nabla d) d\Omega_0 \tag{2.15}$$

where α is equivalent plastic strain and $g_p(d)$ is the plastic degradation function which provides a mechanism for driving crack growth by the development of plastic strains. For the elastic and plastic degradation functions we have presently chosen the form as,

$$g(d) = g_p(d) = (1 - d)^2 + k \tag{2.16}$$

This particular quadratic degradation function is chosen based on the properties as– $g = g_p = 1$ for $d = 0$ and $g = g_p = 0$ for $d = 1$; along with $g'(d) = g'_p(d) < 0$. $k \approx 10^{-8}$ is a small parameter to ensure numerical stability in the computation for a fully damaged element. To compute the effective plastic work contribution for driving the crack growth we consider a simple form as given by,

$$\dot{W}_p = \beta_p(\bar{\tau} \nu^p) \tag{2.17}$$

where $\beta_p \in [0, 1]$ is a scalar factor controlling the percentage of plastic strain contribution into the crack driving force; $\bar{\tau}$ and ν^p are the effective Mandel stress measure

and the equivalent plastic shear strain rate, respectively.

2.2.1 Balance laws

To derive the governing equation for phase-field in a general, thermodynamically consistent approach, we assume the existence of a microforce balance condition describing the kinematics of the phase-field [31, 34, 35, 36]. Starting with the local form of usual linear and angular momentum balance laws we can write,

$$div(\mathbf{T}) + \mathbf{b} = \mathbf{0} \tag{2.18}$$

and the angular momentum balance is enforced through the symmetric property of the Cauchy stress $\mathbf{T} = \mathbf{T}^T$. $\mathbf{b}$ represents the body force vector.

To derive the microforce balance law, we assume that at each time step the phase-field can be characterized by an internal microforce $\pi(\mathbf{x}, t) \in \mathbb{R}$ and a microforce traction vector $\boldsymbol{\xi}(\mathbf{x}, t) \in \mathbb{R}^d$. Assuming all other microforce terms as zero, the balance law can be postulated as,

$$div(\boldsymbol{\xi}) + \pi = 0 \tag{2.19}$$

2.3 Second law and dissipation inequality

Assuming an isothermal process, the rate of change of Helmholtz free energy (ψ) can be written in the form of dissipation inequality as,

$$\rho_0 \dot{\psi} \leqslant \frac{1}{2}\mathbf{S} : \dot{\mathbf{C}} + \boldsymbol{\xi}.\dot{\nabla} d - \pi \dot{d} \tag{2.20}$$

where $\mathbf{C} = \mathbf{F}^T\mathbf{F}$ is the right Cauchy-Green strain tensor and $\mathbf{S} = J\mathbf{F}^{-1}\mathbf{T}\mathbf{F}^{-T}$ is the 2nd Piola-Kirchoff stress tensor. To make the model thermodynamically consistent, one needs to define the free energy ψ such that the above inequality holds. Hence, we assume the free energy function takes the general form as $\psi = \psi(\mathbf{C}, \mathbf{C}^p, \mathbf{Q}, d, \nabla d)$, where $\mathbf{Q}$ is a set of internal plastic variables and $\mathbf{C}^p = \mathbf{F}^{pT}\mathbf{F}^p$ is the plastic right Cauchy-Green strain tensor. Re-writing Eqn.2.20 we get,

$$\rho_0 \frac{\partial \psi}{\partial \mathbf{C}} : \dot{\mathbf{C}} + \rho_0 \frac{\partial \psi}{\partial \mathbf{C}^p} : \dot{\mathbf{C}}^p + \rho_0 \frac{\partial \psi}{\partial \mathbf{Q}}.\dot{\mathbf{Q}} + \rho_0 \frac{\partial \psi}{\partial d}\dot{d} + \rho_0 \frac{\partial \psi}{\partial (\nabla d)}.\nabla \dot{d} - \frac{1}{2}\mathbf{S} : \dot{\mathbf{C}} - \boldsymbol{\xi}.\nabla \dot{d} + \pi \dot{d} \leq 0 \tag{2.21}$$

In order to hold the inequality for any arbitrary deformation history, the following equalities need to be valid,

$$2\rho_0 \frac{\partial \psi}{\partial \mathbf{C}} = \mathbf{S} \tag{2.22}$$

$$\rho_0 \frac{\partial \psi}{\partial (\nabla d)} = \boldsymbol{\xi} \tag{2.23}$$

$$-\rho_0 \frac{\partial \psi}{\partial d} = \pi \tag{2.24}$$

and finally the total dissipation can be written as,

$$\mathbb{D} = -\rho_0 \frac{\partial \psi}{\partial \mathbf{C}^p} : \dot{\mathbf{C}}^p - \rho_0 \frac{\partial \psi}{\partial \mathbf{Q}} . \dot{\mathbf{Q}} \geq 0 \tag{2.25}$$

Eqn.2.22-2.24 represent the thermodynamic constrains for the constitutive equations. Using Eqn. 2.23 and 2.24 we can rewrite the microforce balance eqn. as,

$$div \left(\rho_0 \frac{\partial \psi}{\partial \nabla d} \right) - \rho_0 \frac{\partial \psi}{\partial d} = 0 \tag{2.26}$$

Considering the Helmholtz free-energy as given by,

$$\rho_0 \psi = g(d) W(\mathbf{C}, \mathbf{C}^p) + g_p(d) W_p(\mathbf{Q}) + G_c \left[\frac{d^2}{2 l_c} + \frac{l_c}{2} |\nabla d|^2 \right] \tag{2.27}$$

we can write,

$$\rho_0 \frac{\partial \psi}{\partial d} = g'W + g'_p W_p + G_c \frac{d}{l_c} \tag{2.28}$$

and

$$div\left(\rho_0 \frac{\partial \psi}{\partial \nabla d}\right) = G_c l_c \; div(\nabla d) \tag{2.29}$$

Finally, the microforce balance can be re-written as the governing equation for phase-field evolution as,

$$G_c l_c \; div(\nabla d) - g'W - g'_p W_p - G_c \frac{d}{l_c} = 0 \tag{2.30}$$

In order to enforce the damage irreversibility constraint as $\dot{d} \geq 0$, we further introduce a history functional based on the elastic energy density (following a well known approach by Miehe et al.[33]) as,

$$\mathbb{H} = max_{0<t_s \leq t} < W(t_s) + W_p(t_s) > \tag{2.31}$$

where t_s is the time measure.

2.4 Diffusion-reaction mechanism of pure Mg in a physiological environment

Magnesium is known to be a very reactive material, as it will react with water in any aqueous environment. The reaction produces magnesium hydroxide, which forms a protective surface layer on the magnesium that slows down the reaction. This protective layer is often helpful for biodegradable implant applications, because it allows the implant to last longer than if the reaction were to continue unhindered. The overall reaction can be written as follows:

$$Mg + 2H_2O \longrightarrow Mg(OH)_2 + H_2 \tag{2.32}$$

The reaction in aqueous environment is dominated by the electrochemical coupling between magnesium and impurities or grain boundaries. The Mg matrix acts as an anode while the impurities or grain boundaries act as local cathodes [27]. The overall reaction can be split into the following reactions-

$$Mg \longrightarrow Mg^{2+} + 2e- \text{ (anodic)} \tag{2.33}$$

$$2H_2O + 2e^- \longrightarrow H_2 + 2OH^- \text{ (cathodic)} \tag{2.34}$$

and finally,

$$Mg^{2+} + 2OH^- \longrightarrow Mg(OH)_2 \tag{2.35}$$

The resulting magnesium hydroxide layer forms a protective barrier, however the presence of chloride ions in the physiological environment accelerates the dissolution of this hydroxide layer as follows-

$$Mg(OH)_2 + 2Cl^- \longrightarrow MgCl_2 + 2OH^- \tag{2.36}$$

Based on the prior studies reported in literature, it is assumed that the reactions occur faster than the transport of the reactants in the medium due to diffusion [26, 27]. Therefore, the entire diffusion-reaction process is considered to be a diffusion-controlled process. Considering the fact that the Mg ion concentration in the physiological fluid environment is much lower than the bulk implant, an outward diffusion is considered as,

$$\frac{\partial c_R}{\partial t} = -\nabla \mathbf{j}_R \tag{2.37}$$

in which, c_R is the concentration of the Mg ion and $\mathbf{j}_R$ is the mass flux. To solve this equation we further define a phenomenological constitutive flow equation for $\mathbf{j}_R$. Hence, following Fick's law for the flux of diffusing ions we can write,

$$\mathbf{j}_R = -m\nabla\mu \tag{2.38}$$

where m is the ion's mobility and μ is the chemical potential of the diffusing ion. Further considering an ideal mixing theory, the chemical potential μ can be written as,

$$\mu = \mu^0 + R\theta ln(c_R) \tag{2.39}$$

where μ^0 is the reference chemical potential, R is the universal gas constant and θ is the ambient temperature. Following which, the gradient of μ can be derived as,

$$\nabla\mu = \frac{R\theta}{c_R}\nabla c_R \tag{2.40}$$

Using Eqn.2.40 in Eqn. 2.38 and in Eqn. 2.37 we get,

$$\frac{\partial c_R}{\partial t} = m\frac{R\theta}{c_R}\nabla(\nabla c_R) \tag{2.41}$$

Next, defining the diffusivity parameter as, $D = m\left(\frac{R\theta}{c_R}\right)$, finally we can write

$$\frac{\partial c_R}{\partial t} = D\nabla(\nabla c_R) \tag{2.42}$$

2.4.1 Modification of mechanical properties due to diffusion-reaction

The model assumes that the diffusion-reaction process is isochoric, so that the diffusion of magnesium ions results in a lower concentration of magnesium in the affected areas. A ratio of the current concentration to the original concentration is then defined as,

$$C_{ratio} = \frac{c_r}{c_0} \tag{2.43}$$

where c_0 is the original concentration. Functions were then chosen to modify the fracture energy G_c, the characteristic length scale l_c, and the reference shear strain rate ν_0 as a function of C_{ratio}:

$$G_c = G_{c,0} * e^{-3*(1-C_{ratio})} \tag{2.44}$$

$$\nu_0 = \nu_0 * e^{-10*(1-C_{ratio})} \tag{2.45}$$

$$l_c = 1 + (1 - C_{ratio})^{1/4} \tag{2.46}$$

A visualization of these functions can be found in 2.3, where the multiplier is a function of C_{ratio} (which starts at 1). These functions were chosen because they are continuous on C_{ratio}'s domain of (0,1], and have a significant impact on the property

within the first 20% loss of concentration, which was necessary to have a noticeable effect on the global specimen response. The functions for G_c and ν_0 decrease these values, while l_c is increased by it's function. Simulations were run where other material properties such as h, $\sigma_{y,s}$ and $\sigma_{y,s}$ were modified, however these did not produce desirable results.

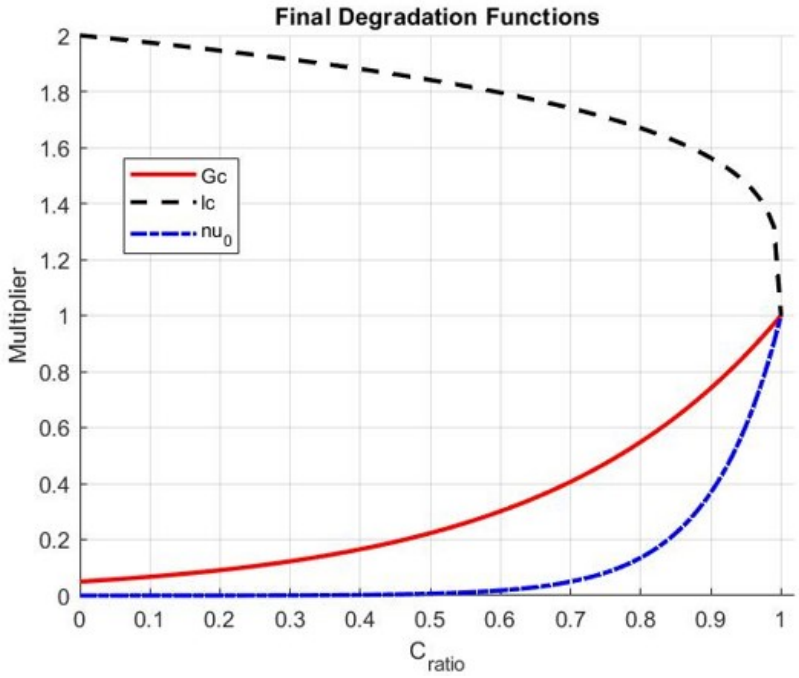

Figure 2.3: Visualization of material property degradation functions.

2.5 Numerical Implementation

The proposed constitutive model is implemented in a commercial finite element package ABAQUS/Standard by writing a User Element (UEL) Subroutine to solve for the

mechanical displacement, Mg ion concentration and phase-field evolution. A monolithic solver is considered to solve for the nodal displacement and phase-field damage. For the diffusion (mass transport) equation, since the time scale is much larger two step solutions are adopted, where the first step considered the diffusion boundary conditions over a larger time period and the mechanical displacement boundary conditions are applied in the following step. For the finite element implementation, the governing equations are discretized based on their (variational) weak form. Herein we highlight the steps for the FEM discretization as follows- The body is approximated using finite elements as $\Omega = \cup\Omega_e$. Following which, the nodal displacement vector $\mathbf{u}$, nodal damage d, and Mg concentration c_R^{Mg} are approximated within the element using interpolating (shape) functions N^A as,

$$\begin{aligned} \mathbf{u} &= \sum_{A=1}^{n} \mathbf{u}^A N^A, \\ d &= \sum_{A=1}^{n} d^A N^A, \\ c_R^{Mg} &= \sum_{A=1}^{n} c_R^A N^A \end{aligned} \tag{2.47}$$

Where A denotes the node number. The weak form of the governing equations with the finite element approximation can be then written as,

$$\begin{aligned}
\int_{\Omega}\left(\mathbf{T}_R : \frac{\partial N^A}{\partial \mathbf{x}}\right)dV &= \int_{S_2}\left(N^A \check{\mathbf{t}}_R\right)dA, \\
\int_B\left(\frac{g_c}{l_c}[(\Delta d)l_c^2 - d]\right)dV &= -\int_B\left(g'W + g'W_p\right)dV, \\
\int_B\left(N^A c_R^{Mg} + \mathbf{D}\frac{\partial N^A}{\partial \mathbf{x}}\frac{\partial c_R^{Mg}}{\partial \mathbf{x}}\right)dV &= -\int_{S_{\mathbf{j}_R}}\left(N^A \check{j}_R\right)dA
\end{aligned} \tag{2.48}$$

where B represents the domain and S represents the surfaces where the traction boundary conditions are specified respectively. Following which the system of equations are solved using an iterative Newton solver, with the element level residuals are given in the form as,

$$\mathbf{R}_{\mathbf{u}}^e = -\int_{\Omega}\left(\mathbf{T}_R : \frac{\partial N^A}{\partial \mathbf{x}}\right)dV + \int_{S_2}\left(N^A \check{\mathbf{t}}_R\right)dA,$$

for the displacement residual,

$$\mathbf{R}_d^e = -\int_B\left(\frac{g_c}{l_c}[(\Delta d)l_c^2 - d]\right)dV - \int_B\left(g'W + g'W_p\right)dV,$$

for the phase-field residual,

$$\mathbf{R}_c^e = -\int_{B^e}\left(N^A c_R^{Mg} + \mathbf{D}\frac{\partial N^A}{\partial \mathbf{x}}\frac{\partial c_R^{Mg}}{\partial \mathbf{x}}\right)dV - \int_{S_{\mathbf{j}_R}}\left(N^A \check{j}_R\right)dA \tag{2.49}$$

for the Mg concentration, respectively.

Finally, the tangents for Newton solver are defined as,

$$K_{\mathbf{uu}}^{AB} = -\frac{\partial \mathbf{R}_{\mathbf{u}}{}^{A}}{\partial \mathbf{u}^{B}} \ , \ K_{dd}^{AB} = -\frac{\partial \mathbf{R}_{d}{}^{A}}{\partial \mathbf{u}^{B}} \ , \ K_{cc}^{AB} = -\frac{\partial \mathbf{R}_{c}{}^{A}}{\partial d} \tag{2.50}$$

Chapter 3

Experimental Methods

3.1 Material Characterization

To validate the model, experiments were completed using 99.9%+ purity magnesium (commercial purity). Drawn magnesium rods 7.9 mm in diameter from Goodfellow Corp. (Figure 3.1a) were machined into round tensile specimens (b). These tensile specimens had a 3 mm diameter gauge section and 16 mm gauge length (approximately proportional to ASTM E8M standard round specimen). The tensile specimens were then annealed at 400 C for 24 h. The goal of this treatment was to initiate recrystallization in the magnesium, in order to obtain larger grains and fewer grain boundaries. This was done to minimize the number of grains and grain boundaries,

so that the boundaries wouldn't impact the corrosion as much and because the model is phenomenological and does not contain any crystallographic information.

(a) (b)

Figure 3.1: (a) Magnesium rods as received and (b) the prepared tensile specimens.

3.1.1 Metallography Preparation

To assess the effects of the annealing treatment, metallography was done on an un-annealed and annealed section of rod to observe the difference in grain structure.

Pieces of rod were mounted in epoxy and then polished by hand on a wheel. Due to magnesium's soft nature, SiC paper was avoided to prevent buildup of SiC particles in the sample surface. Firstly, MD-Piano discs of grit 500 and 1000 (Struers) were used even out the surface and begin polishing. For the next two steps, 3 μm and 1 μm DiaLube Diamond Suspensions (Allied High Tech Products) were used on cloth pads. The final polish was achieved with using a 0.04 μm Colloidal Silica Suspension (Allied High Tech Products) on a cloth pad. Samples were cleaned with soap and ethanol between each step, and were cleaned in ethanol with an ultrasonic cleaner between the diamond paste and silica polishing stages. The final polish had to be kept short because of the Mg's softness, as the sample would start collecting silica particles around the edges if polished for too long. For the optical microscope images, after polishing the samples were etched in ethyl glycol for one minute to make the grain structure more visible.

3.1.2 Metallography Results

3.1.2.1 Optical Microscope Images

Before annealing, there were a many long twin grain boundaries near the edge of the sample (Figure 3.2), which were likely due to the deformation experienced by

the edge of the rod during the drawing process. Quite a few of these twins extend into neighboring grains, which isn't ideal because these adjoining twin pairs can promote crack nucleation [37].. After annealing the twins seemed to be smaller and concentrated in some grains, however almost all the twins appeared to stop at the grain boundaries. The average grain size also appears to be a bit larger, but this will be quantified later.

Looking at the images from the center of the rod in Figure 3.3, there seems to be a similar trend to the edge. While the center didn't have as many twins as the edge, those present before annealing were long and a few extended into other grains. After annealing, the twins were again concentrated in just some of the grains, and they don't seem to extend into other grains. One interesting observation was that after etching the annealed sample, a large grain several mm in length could be seen without any instruments (Figure 3.4). It is possible that there was a higher amount of plastic deformation in that area during the drawing process, which led to more recrystallization and the formation of a large grain.

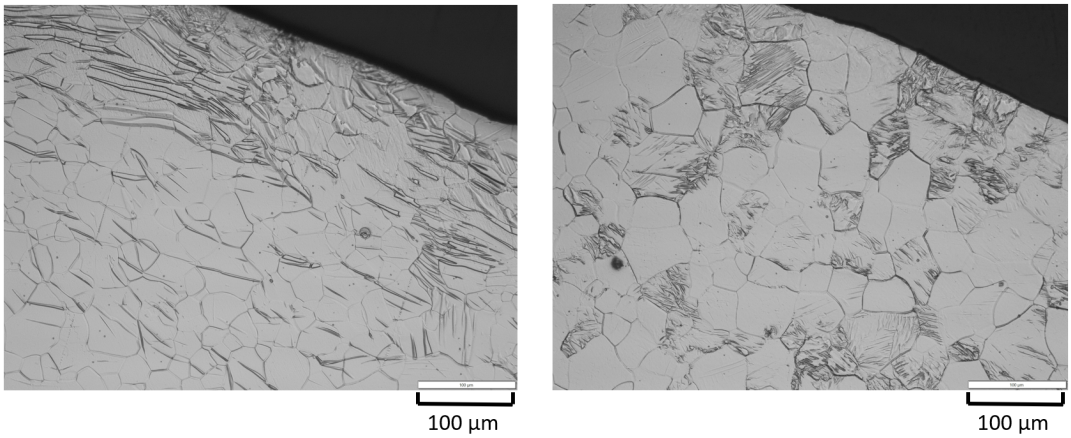

(a) Before annealing (b) After annealing

Figure 3.2: Optical microscope images of grain structure near edge of rod (transverse cut, 100x).

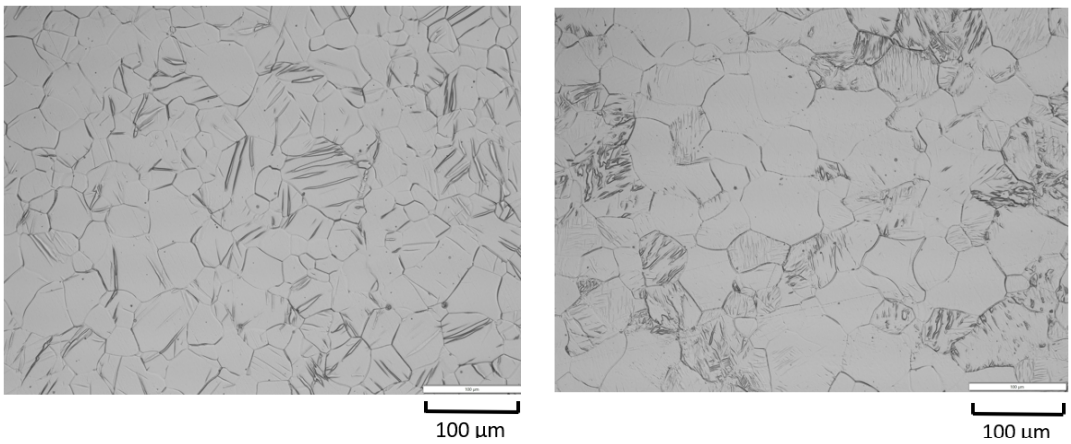

(a) Before annealing (b) After annealing

Figure 3.3: Optical microscope images of grain structure in center of rod (transverse cut, 100x).

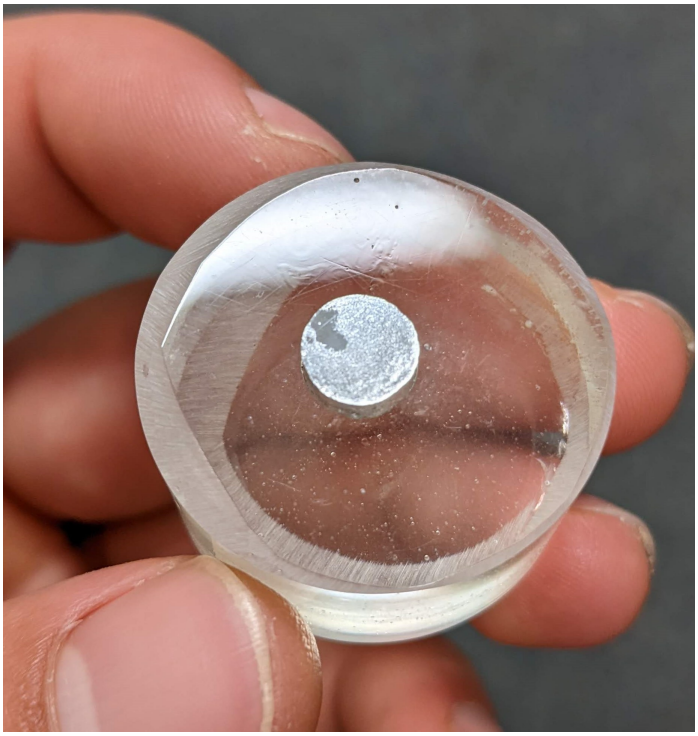

Figure 3.4: Large grain visible after etching (seen top left of the rod cross section, which is mounted in epoxy).

3.1.2.2 EBSD Results

After the optical images were captured, the samples were re-polished and then broken out of the epoxy to be looked at using a Philips XL40 scanning electron microscope (SEM). Cutting the samples out of the epoxy usually ruined the surface finish, so the final polishing step had to be repeated after they were broken out. In the SEM, electron backscatter diffraction (EBSD) was used to identify crystallographic information such as grain size and orientation. An accelerating voltage of 20kV was used, and images were captured at 250x magnification, although their legends may differ slightly due to differences in the working distance.

Figure 3.5 shows inverse pole figure (IPF) maps of the samples before and after annealing. These maps color code the grains based on their orientation, and they can be decoded with the legend (c). It can be seen that the edges have a very strong grain orientation preference, since they are mostly greens and blues. Similar to the frequency of twins described earlier, this orientation preference is likely due to the deformation that occurred at the edges during the drawing process. Some twins are visible as streaks of colors in these images, but they don't show up as well as the optical images.

The center of the samples on the other hand have a variety of colors in their IPF plots (Figure 3.6), which indicates that there is not much of a preference to one grain orientation. This center grain structure should be more representative of the

tensile samples' gauge section, since they were machined out of the rods on a lathe. While this crystallographic information was not incorporated into our current model, it could be used as a starting point for future physical models.

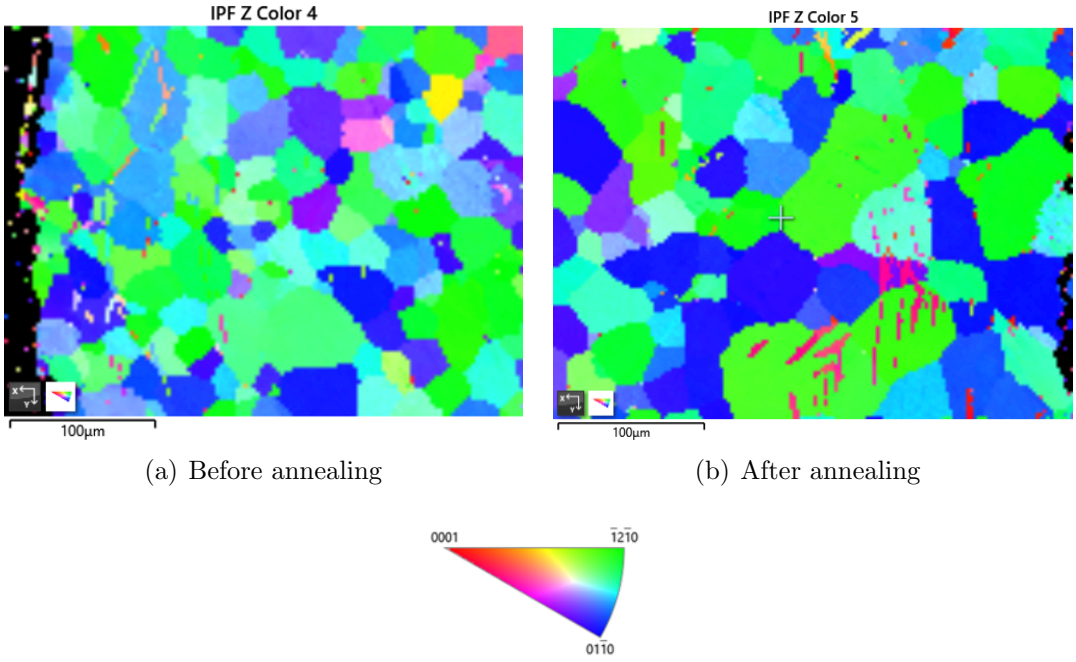

(a) Before annealing

(b) After annealing

(c) IPF legend

Figure 3.5: EBSD Inverse Pole Figure (IPF) results near the edge of rod at 250x (transverse cut, normal direction).

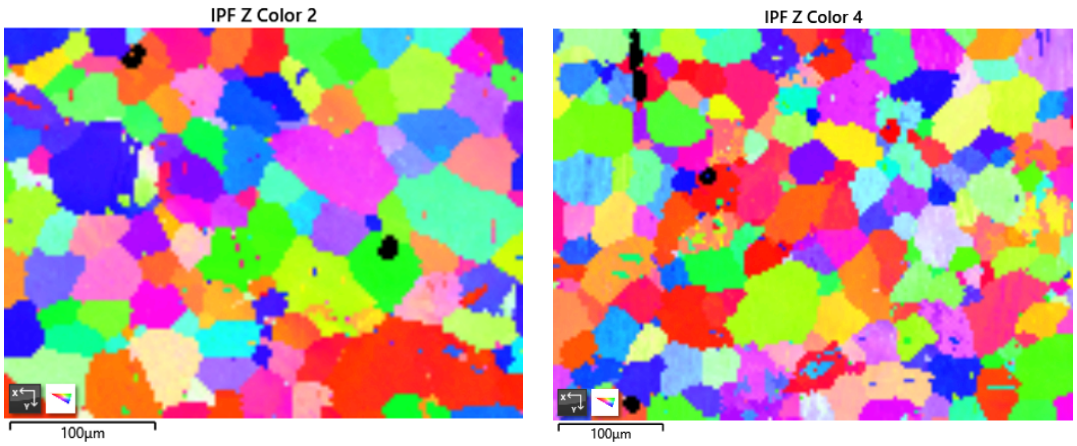

(a) Before Annealing (b) After Annealing

Figure 3.6: EBSD IPF results in the center of the rod at 250x (transverse cut, normal direction).

Table 3.1
Grain length statistics from EBSD

		Area (μm)			
Annealing	**Location**	**Min**	**Max**	**Mean**	**SDV**
Before	Center	14.0	126.5	39.8	17.8
	Edge	12.5	97.8	35.8	16.7
After	Center	16.7	113.9	44.8	18.9
	Edge	10.6	87.1	39.1	20.0

3.2 Mechanical Testing Procedures

After annealing, the gauge sections of all the tensile specimens were polished using 600 and 1000 grit SiC paper. They were then cleaned using acetone in an ultrasonic cleaner for five minutes. After this point the gauges of the tensile bars were only touched with latex gloves to prevent any contamination on the surface. Next, the

grips of the specimens undergoing no-load immersion in HBSS were wrapped in 3M Super88 vinyl tape and then shrink wrapped with tubing to protect them from corrosion as shown in Figure 3.7. This ensured that only the gauge section would be weakened by the HBSS. Specimens were then placed in 50 mL vials of HBSS, and these vials were placed in a water bath to maintain a temperature of 37 C plus/minus 1 degree. The HBSS used was a premixed solution from Sigma Aldrich (mixture H8264), for which the composition can be found in Table 3.2.Samples were immersed for two periods of time: 5 h or 10 h. After the corrosion bath was over, the samples were briefly rinsed with distilled water and then air dried.

Table 3.2
Hank's Balanced Salt Solution composition.

Component	**g/L**
$CaCl_2$	0.185
$MgSO_4$	0.09767
KCl	0.4
KH_2PO_4	0.06
$NaHCO_3$	0.35
NaCl	8.0
Na_2HPO_4	0.04788
D-Glucose	1.0

For the first set of tensile tests, a Instron 4206 test system with a 300 lb load cell (Futek) was used. A 10 mm extensometer (Epsilon) was used to measure the strain, and specimen diameter was measured after immersion for the stress

Figure 3.7: Tensile samples after 5 h in HBSS.

calculations. Three specimens were tested for each of the three following scenarios: uncorroded samples, 5 hr immersion in HBSS, and 10 hr immersion in HBSS. These tests were carried out at a crosshead displacement rate of 0.05 in/min (1.27 mm/min).

The second set of tests were slow strain rate tests (SSRT) completed on an Instron 4210 machine with the same 300 lb load cell. These tests were completed at a much slower crosshead displacement rate of 1 micron per minute, for an approximate strain

rate of $10^{-6}s^{-1}$. Admittedly, these weren't true SSRT tests since it was a constant displacement, but the corrosion chamber used didn't allow for an extensometer to control the strain rate. Two specimens were tested in air, and three were tested using the corrosion cell shown in Figure 3.8, but the first test in the cell was messed up due to frictional forces in the cell. This setup circulated HBSS through the cell and into a 37 deg C bath to maintain a steady temperature throughout the test. To overcome the friction forces in the corrosion cell, the immersed samples were preloaded to 30 lbf at the start of the test to ensure that the tensile specimen was bearing the load as soon as the test started. The in-air tests were completed before this frictional force was realized, so they were only preloaded to 20 lbf.

Additionally, mass loss corrosion tests were attempted in order to approximate the corrosion rate for the model. However, the measured mass loss was negligible when weighed to the thousandth of a gram, so no data was collected for the model. For the attempted tests, pieces of the magnesium rod were machined down to a diameter of 4 mm and cut into 10 mm long pieces. They were then annealed and polished following the same procedure as the tensile bars. These pieces were then hung in the same 50 mL vials using fishing line, and placed in the water bath alongside the tensile specimens. These samples had an approximate surface area of 150 mm^2, which satisfies the ASTM G31 recommendation for the minimum solution volume to specimen surface area ratio of 0.20 mL/mm^2. Once removed from the HBSS, the samples rinsed in water and air

dried before weighing. Had there been a measurable mass loss, the samples would have been placed in chromic acid to dissolve any corrosion products and get a more accurate mass.

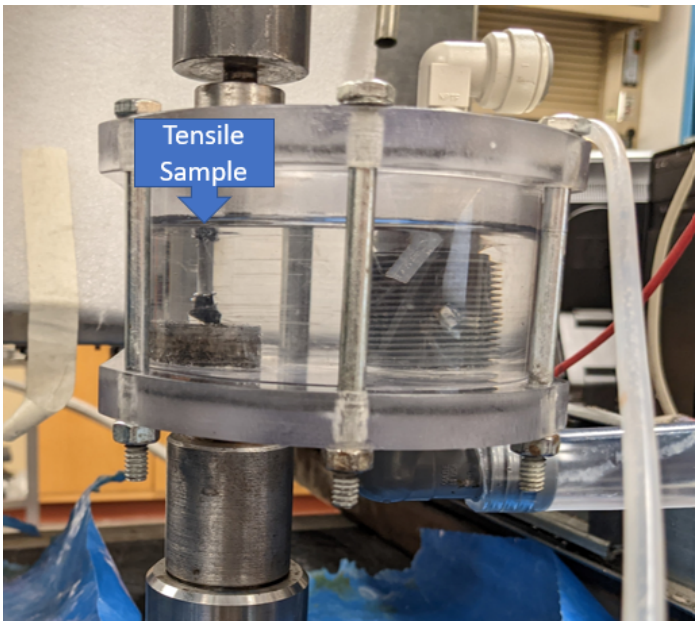

Figure 3.8: Corrosion chamber used for SCC tests.

Chapter 4

Results

4.1 Experimental Results

Based on the data from the standard tensile tests (Fig. 4.1), there was a noticeable drop in the ultimate strength and ultimate strain of the tensile specimen after just five hours of exposure to HBSS. These specimens displayed a similar response to the baseline specimens up until yielding, however they failed soon after the plastic hardening began. However, the samples with 10 hours of pre-exposure displayed no significant change in their response. The initial assumption was that the longer waiting period (2 or 3 weeks) between polishing the surface and immersing in HBSS might have promoted the reaction of Mg with water in the air resulting in a protective

oxide film. Another set of 10 h tests were completed where the samples were put into the solution shortly after polishing, but they still didn't show any significant change in strength. It was concluded that the 50 mL solution was becoming saturated with either Mg or hydrogen gas, preventing further reaction.

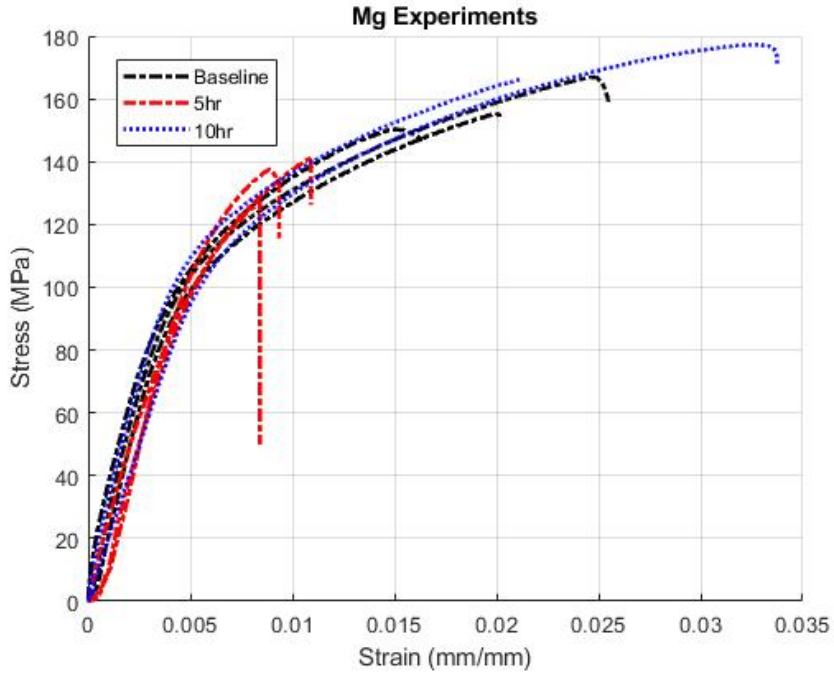

Figure 4.1: Initial experimental results.

Fig. 4.2 shows the results of the slow strain rate tests. Since an extensometer couldn't be used in conjunction with the corrosion cell, the load-displacement curves are plotted instead of the stress-strain curves. For reference, the in-air tests took about 22 hr while the immersion tests took 9hr. While in the standard tensile tests the only significant difference observed was near the failure point, in the SSRT tests the immersed samples also yielded much sooner than the in-air tests. After yielding,

they failed at a much lower load and they didn't display much hardening. All of these changes indicate that Mg is susceptible to stress corrosion cracking (SCC). One of the immersion tests also displayed a different stiffness than the other three tests, however it is possible this was due to the varying frictional force in the corrosion cell. While limited, these SSRT tests provide a reference point for how Mg behaves when loaded in a corrosive environment.

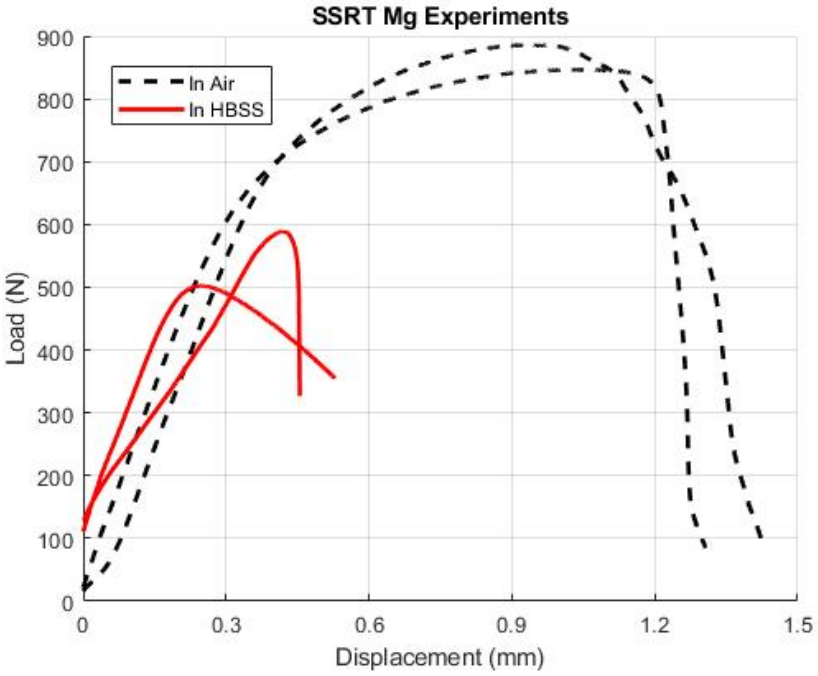

Figure 4.2: Slow strain rate tensile test results.

Due to the lack of change in properties for the first two 10 h immersions, another test was completed following the same procedure, however each sample was placed in its own 200 mL jar of solution instead of a 50 mL vial. After 10 h, the sample surfaces looked about the same as the other 10 h tests, so 100 mL of solution was changed

and the samples were left for an additional 17 h. At this cumulative time of 27 h, the samples were removed from the solution for testing. The results in Figure 4.3 indicate that the samples yielded a little earlier, but experienced a similar strain at failure.

In order to test the theory that the solution was becoming saturated with Mg or hydrogen, a fresh dogbone was placed in the solution from a 27 h specimen. Within 15 s it began bubbling, indicating that the solution still had the potential for reaction. Therefore, it appears that some tests produced a more protective oxide layer than others. A possible explanation for this is that there were differences in the tensile specimen microstructures, despite all specimens being made from the same batch of Mg rods. It is also possible that the polishing technique was different for the later batches of tests, however this wouldn't explain why the initial 10 h tests showed minimal change despite being polished at the same time as the 5 h samples. This issue of varying corrosion rates remains unsolved in the present work, and should be investigated in future works

Since the change in mechanical properties was still inconsistent, five samples were tested that had been immersed in HBSS for 24 h earlier in the project. These samples underwent the same preparation as the others, except that they were immersed in HBSS at room temperature. They had previously been set aside due to the extreme

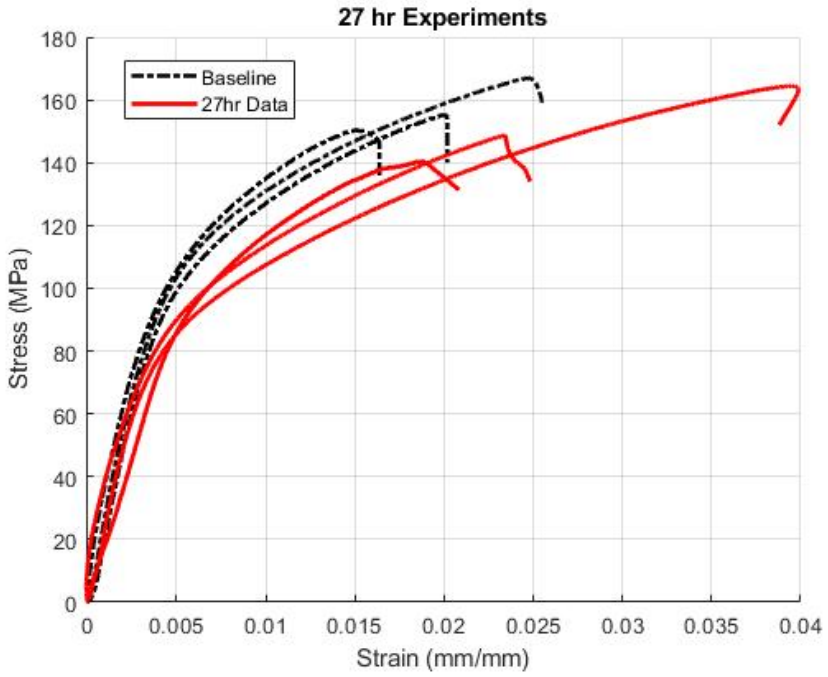

Figure 4.3: Tensile test results for specimens immersed in HBSS for 27 h.

corrosion they experienced, as seen in Figure 4.4. When testing these samples, the unevenness of the gauge sections prevented accurate extensometer results and measurement of the cross section area. Therefore, load-displacement curves were plotted instead of stress-strain curves. As expected, there was a significant drop in the stiffness, yield strength, ultimate tensile strength, and elongation at failure of these severely corroded samples (Figure 4.5).

Figure 4.4: Tensile specimens after 24 h in HBSS.

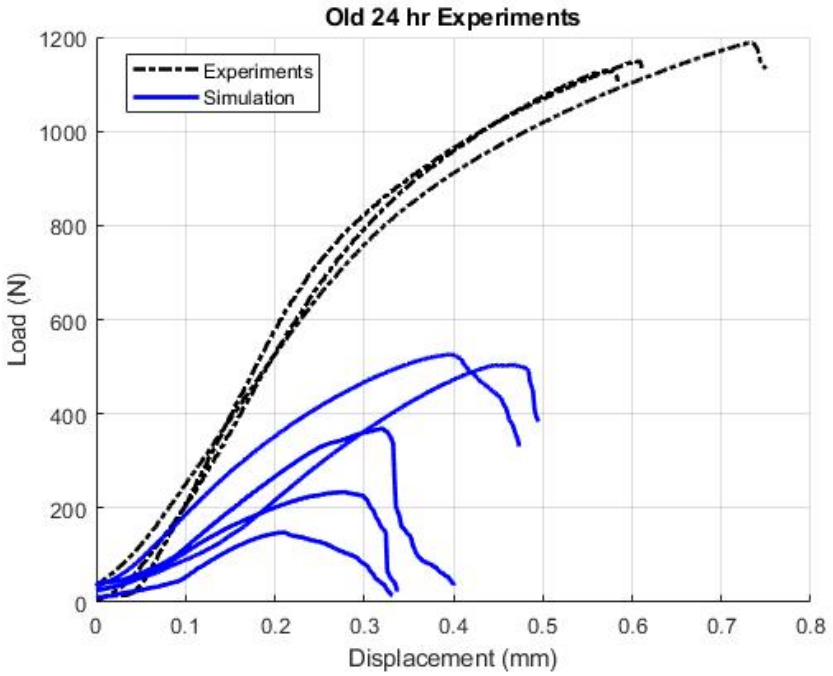

Figure 4.5: Tensile test results of severely corroded specimens.

4.2 Numerical Simulations

4.2.1 Model Exploration

Alongside with the experiments, considerable work was done developing and exploring the capabilities of the proposed model. Initial simulations were done to conduct a parametric study exploring the influence of the two phase-field parameters l_c (characteristic length) and G_c (critical fracture energy) on the final load-displacement response of the materials. Simulations were performed to emulate tensile tests on a simple 2D dogbone geometry. Based on the results plotted at Figure 4.6, it can be seen for a constant l_c, a higher G_c would allow the specimen to withstand a larger load (higher strength). This is intuitive as one would expect that a larger fracture energy will provide more resistance to crack growth and thus will increase the peak load/strength of the material. On the other hand the effect of l_c is the opposite on the load-deformation response. For a constant G_c, a higher l_c shows lesser peak load indicating an earlier failure. This is because the parameter l_c controls the phase-field crack width (width of the diffused damage zone) - so the larger l_c is, the greater the width of the diffused damage zone- as a result a larger area is being considered to dissipate the energy required for the crack growth. Hence, a larger l_C will ultimately lead to a lower peak load. However, it is important to note that the phase-field

fracture theory requires the width of the diffused damage zone to be as small as possible, such that $l_c \to 0$ ultimately converges to a sharp crack geometry. Hence, a reasonable l_c value was chosen for the subsequent simulations.

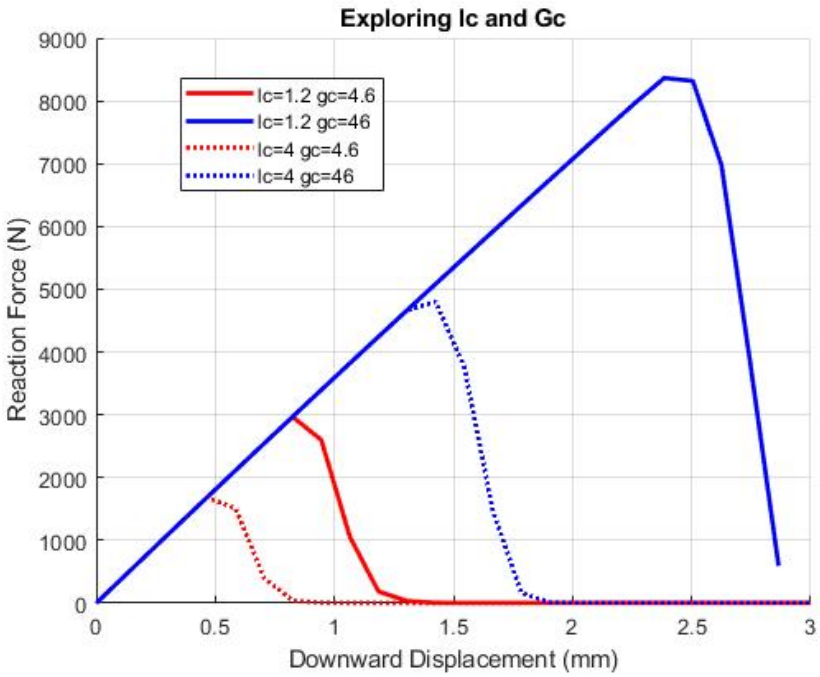

Figure 4.6: Effect of changing l_c and G_c.

The next task was to compare a 2D (plain strain; i.e. zero strain in the out-of-plane direction) and a 3D simulation of a dogbone. These two simulations used the exact same geometry and mesh, except that the 3D simulation had an out-of-plane thickness of 6 mm (and 12 finite elements) to it. All material properties, the displacement increment and the total applied displacements were also the same. A third simulation was also considered where the plastic work weight $beta_p$ was set to zero; disabling its contribution to the phase-field damage evolution. Figure 4.7 shows

that the 2D simulation had a slightly stiffer and brittle response than the 3D one. It also shows that without the plastic work contribution the 3D simulation doesn't show fracture in the specimen. This is likely because once the specimen enters into the plastic regime (beyond yielding), most of the energy is coming from the plastic work instead of the elastic deformation. This simulation illustrates why one needs to incorporate the plastic energy contribution for the evolution of the phase-field damage for a ductile metal like Mg.

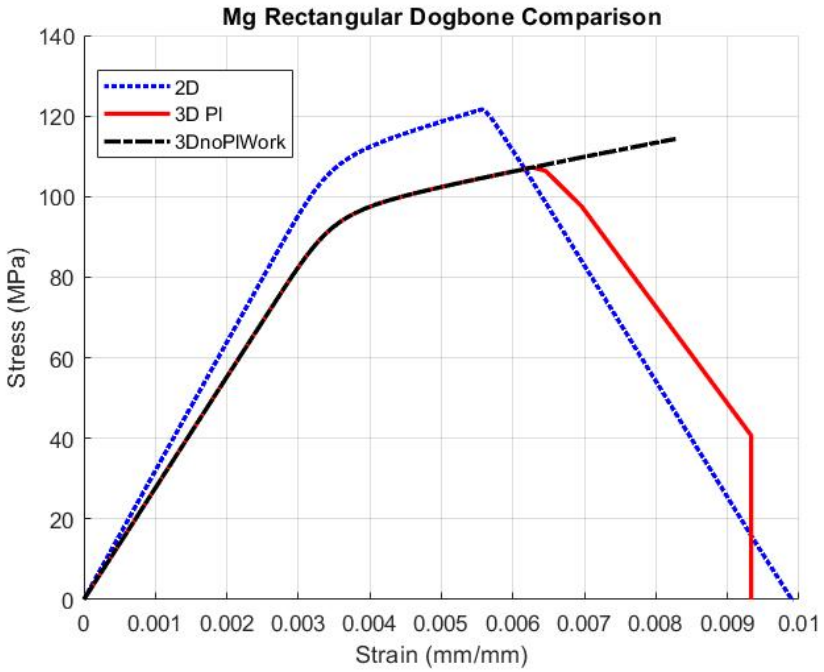

Figure 4.7: 2D and 3D rectangular dogbone comparison.

To simulate the tensile testing, a 3D model of a one eighth section of a round tensile specimen was considered (Figure 4.8). The 3D model was chosen to compare with the exact geometry used in the experiments and it would be difficult to represent

a round cross section in a 2D plain strain model. Only one eighth of the geometry was considered by exploiting the symmetry boundary conditions on the three faces as shown in Figure 4.8. The default Abaqus/Standard YSYMM and ZSYMM boundary conditions could not be used because they set the nodal degree of freedom "4" (related to rotations) to zero. However, in the present numerical implementation nodal d.o.f "4" is used to track the phase-field damage evolution following the differential Eqn.2.28. Hence, the symmetry boundary conditions was chosen as shown in the figure representing the required constraints in the geometry. Diffusion was incorporated by setting a Mg concentration boundary condition on the outer surface of the specimen's gauge length, which represents the Mg concentration of the surrounding fluid around the implants. The core of the implants and everywhere else assumed to have an initial concentration of Mg ions in the solids.

With the 3D geometry developed, the next important step was to do a max step size convergence study. For this the max allowable step was decreased until there wasn't a significant change in the results. In this case, it was determined that a max step size of 0.13 μ produced accurate results, without being too computationally expensive.

Another important task from this case study was to observe how degrading the individual material properties would affect the simulated load displacement curve of the tensile specimen. Figure 4.10 shows a comparison of the simulated load-displacement curves where the samples has no exposure to HBSS to those where the yield strength,

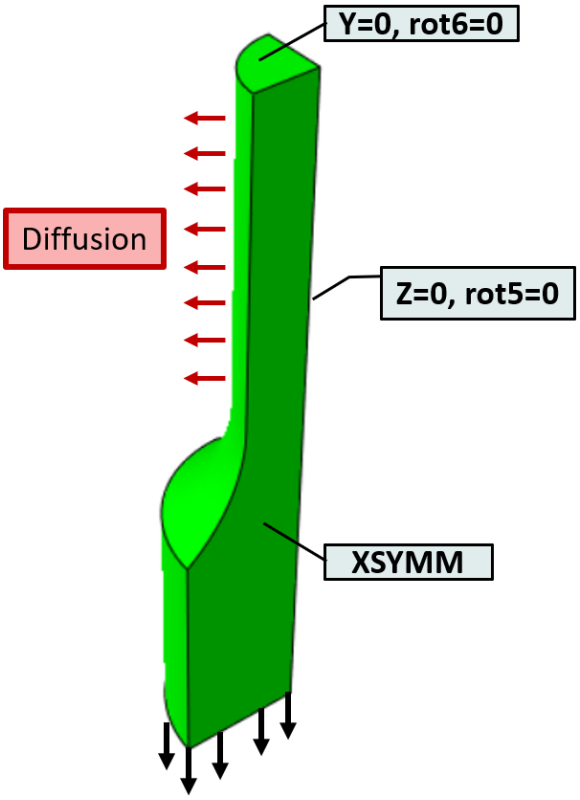

Figure 4.8: Round tensile specimen geometry with boundary conditions.

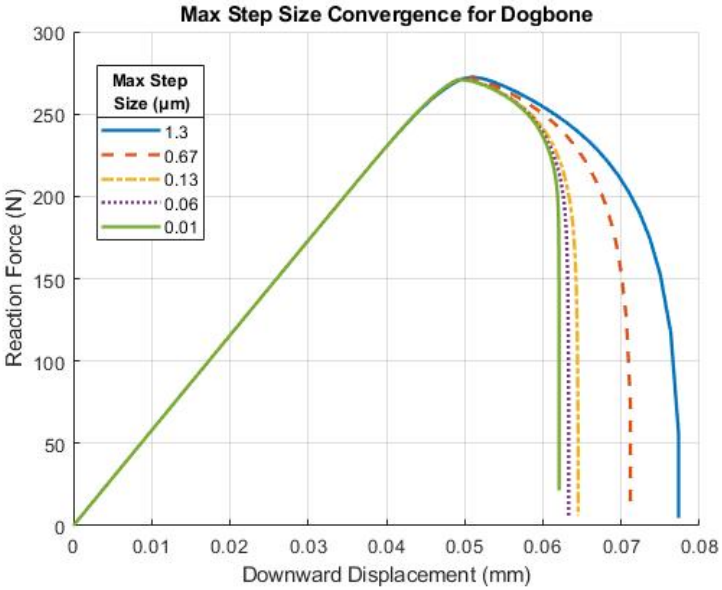

Figure 4.9: Simulation step size convergence.

UTS (ultimate tensile strength), or Gc (critical energy release rate) were degraded by exposure. This plot served as a reference for how to simulate the effect of changes in the important material parameters to compare with the experiments.

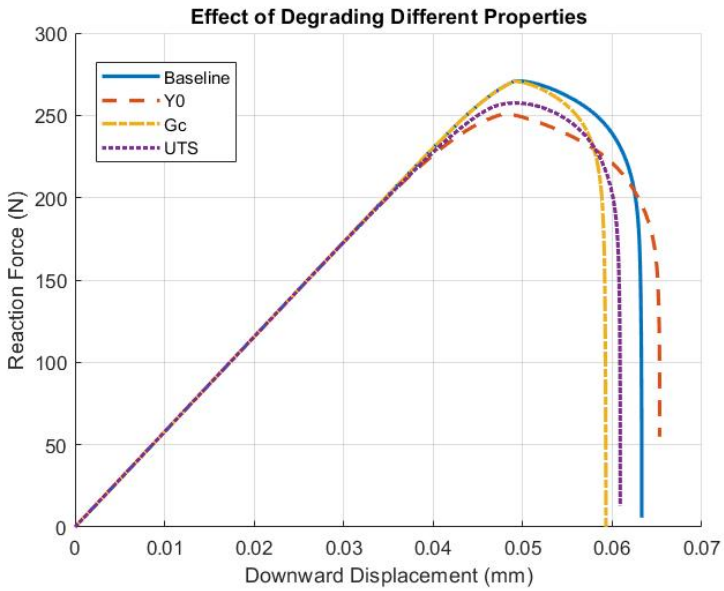

Figure 4.10: Degradation of different properties.

4.2.2 Model Validation

Based on the experiments, the model material parameters were calibrated for the subsequent simulations. The first step was to match the baseline (virgin samples) experiments by tuning the elastic-plastic parameters in the model. The calibrated

parameters are given in Table 4.1. The phase-field variables l_c and G_c were also determined at this stage, although ideally fracture experiments would've been performed to better determine G_c. The simulation of the virgin sample produced a stress-strain curve that matched the experiments well (Figure 4.11.

Table 4.1
Pure Mg material properties determined from mechanical testing.

Bulk modulus (K)	31.1 GPa
Poisson's ratio (ν)	0.35
Shear modulus (G)	10.4 GPa
Yield stress (σ_y)	60 MPa
Hardening modulus (H)	17
Saturation stress ($\sigma_{y,s}$)	160
m	0.22
Shear strain rate (ν_0)	0.001
Length scale parameter (l_c)	0.56
Fracture energy (G_c)	2.8

Next, a simulation was run where the specimen underwent diffusion for 5 h before a tensile test was completed. The model matched the change in ultimate tensile strength reasonable well, however there was significantly more elongation till failure than in the experiments. It was determined this could not be alleviated, because a large portion of the cross section remains unaffected by the diffusion in the current model. Furthermore, the round tensile specimen model does not have any stress concentrations that would help promote crack growth. Figure 4.12 illustrates how as the load is applied, uniform damage is seen around the outer edge of the specimen where G_c has been degraded, but because of the damage uniformity a crack does not

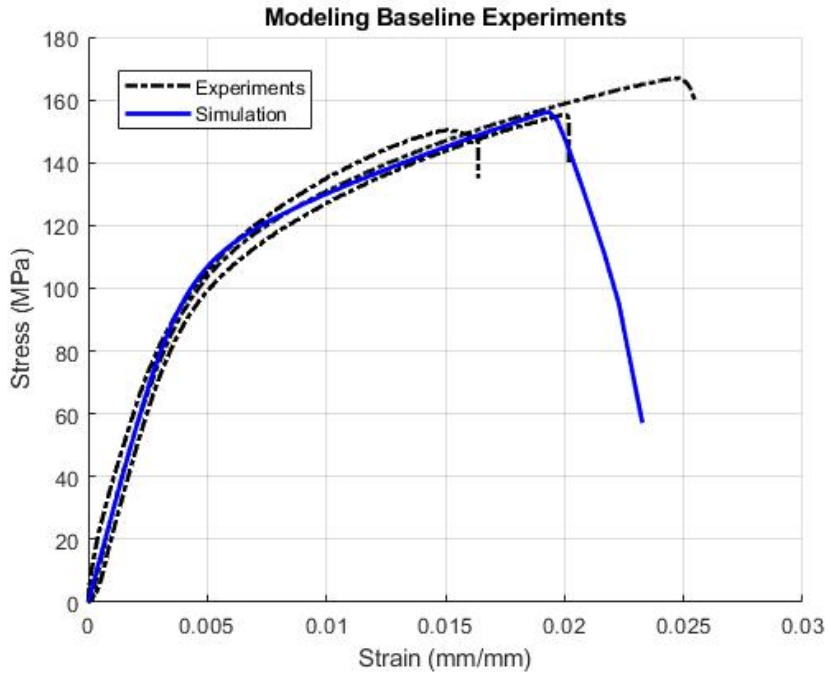

Figure 4.11: Modeling of the baseline tensile tests.

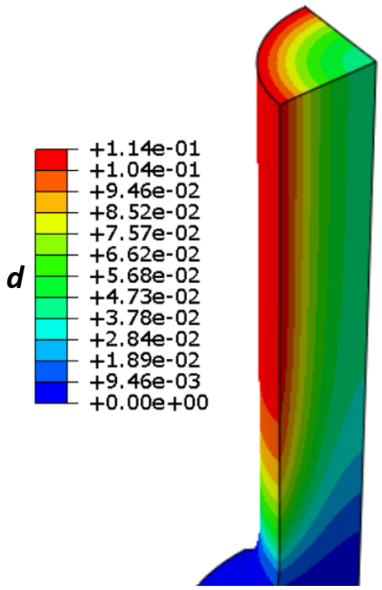

Figure 4.12: Damage contour of degraded round tensile specimen, after a displacement has been applied.

grow into the center. Therefore, this portion of the cross section behaves the same regardless of the properties changed by diffusion. In order to better reflect the failure that was seen in the round specimens, the addition of crack initiation sites via pitting corrosion or crystallographic information will likely be required.

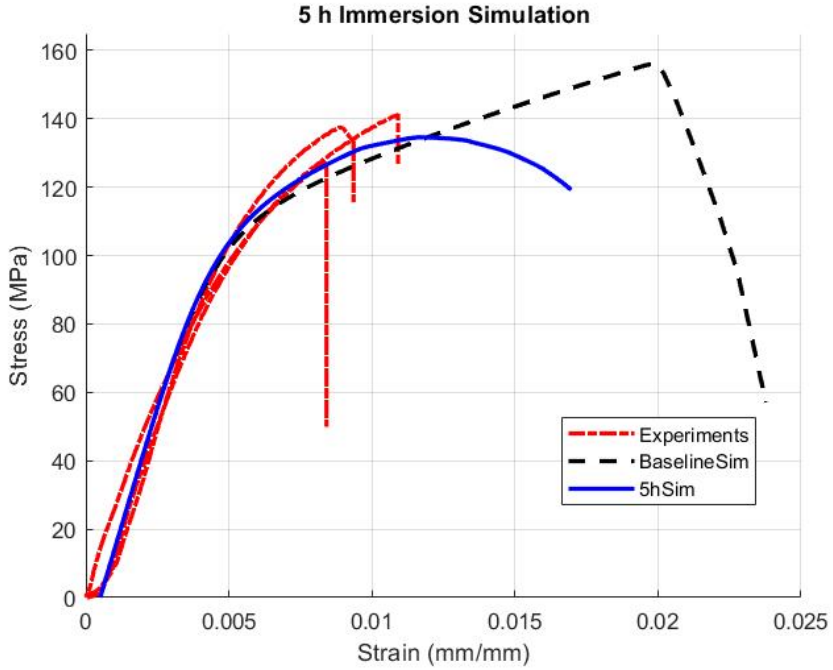

Figure 4.13: Simulation results for specimen immersed for 5 h. Baseline simulation included for reference.

For the third set of mechanical tests to model, the 24 hr set was chosen because they best matched the drop-off in strength seen after 5 hr. Figure 4.14 shows that the model struggled to capture the significant change in strength seen in the specimens after 24 hr. Similarly to the 5 hr specimens, this is likely due to the fact that significant pitting occurred in the test samples, which the current model is not able to capture. These pits were large enough to both reduce the cross section size and serve as crack

initiation sites, which led to failure at a much lower load than that predicted by the model. The model did predict a lower displacement (and therefore strain) at failure than the experiments, which is likely due to the compliance in the testing machine which was not accounted for. Had this been measured it is possible that the model's prediction of ultimate strain would be close to that seen in the experiments.

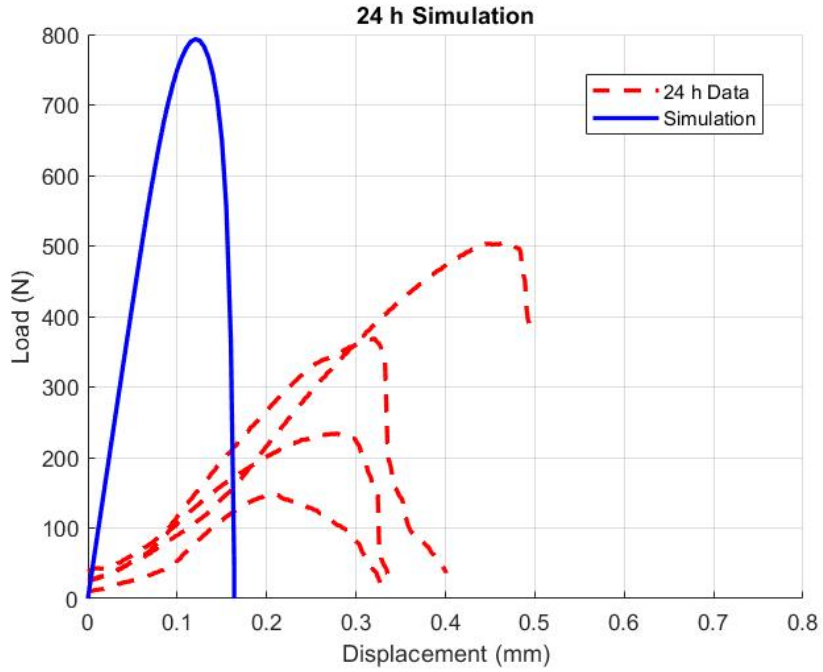

Figure 4.14: Simulation results for specimen immersed for 24 h.

4.2.3 Cracked Plate Simulations

Once the model was calibrated, simulations were ran of a 2D plate with a pre-existing crack pulled in tension (Figure 4.15(a)) and in simple shear (Figure 4.15(b)) to observe how the phase-field fracture model predicted the crack growth in two different loading

conditions. These simulations used the same material properties listed in Table 4.1. For the plate in tension, the crack continued to propagate in the horizontal direction (4.16), while the crack propagated in a declined manner for the plate pulled in shear (4.17). Figure 4.16(b) illustrates how as the crack grows, the stress concentration stays at the tip of the phase-field crack.

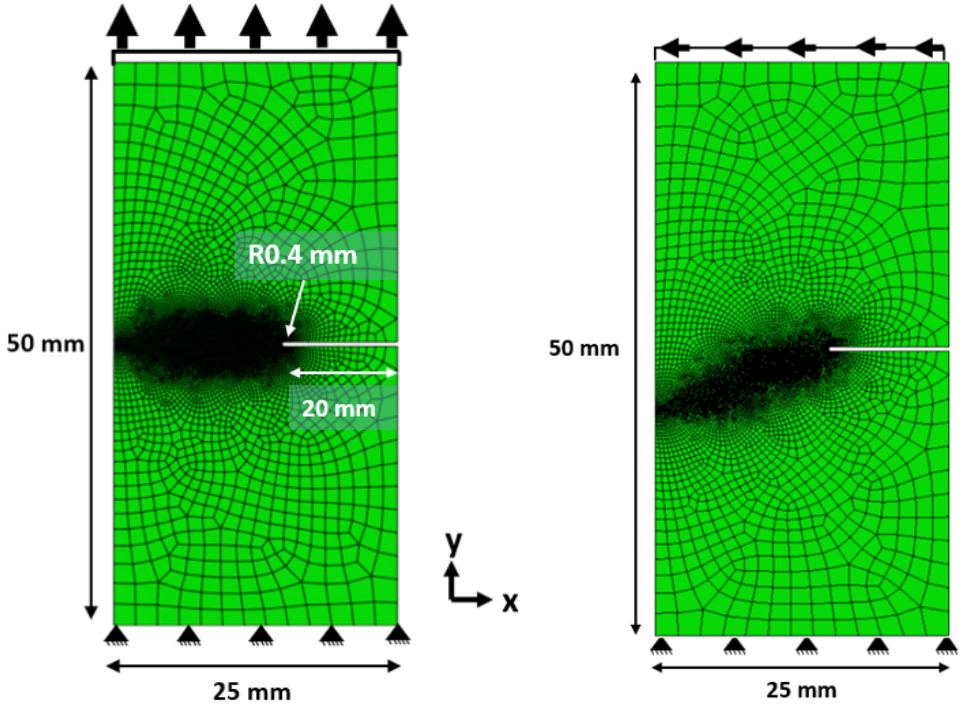

(a) Tension (b) Simple Shear

Figure 4.15: Boundary conditions for pre-cracked plates.

Since the model struggled to predict early fracture due to degradation for the round tensile specimen, the concentration boundary condition was also applied to the edges of the cracked plate geometry, including the crack surface as shown in Figure 4.19 The goal of this was to see if degradation coupled with a stress concentration would result in significantly earlier fracture. It was found that for the cracked plate pulled

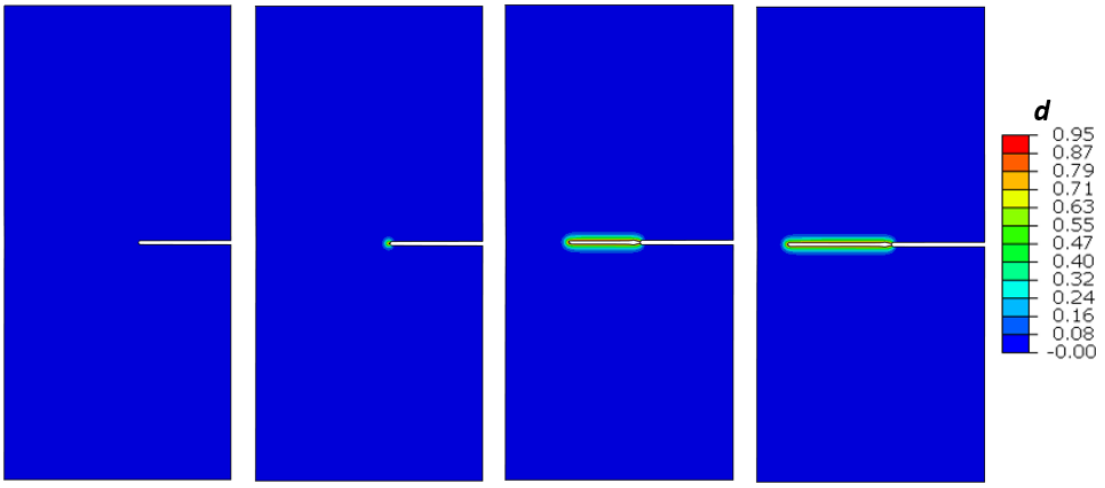

(a) Phase-field crack growth

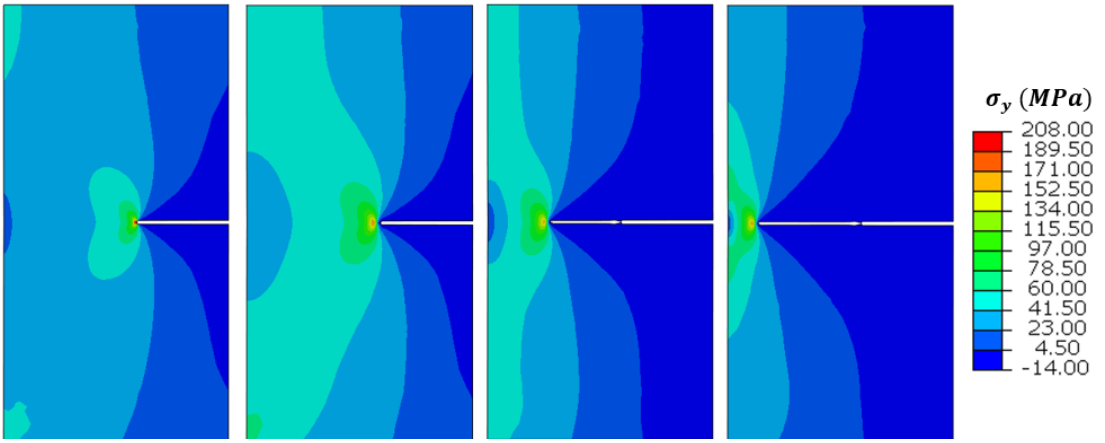

(b) Y-direction stress

Figure 4.16: Crack evolution for pre-cracked plate in tension.

in tension, the maximum load dropped by 7.5% after 5 hr of immersion and 92% after 24 hr, as shown in Figure 4.19. While the percent drop in load of the cracked plate cannot be directly correlated with the drop-off seen in the round tensile specimens, these simulations indicate that the model will predict a significant drop-off when degradation is coupled with a stress concentration.

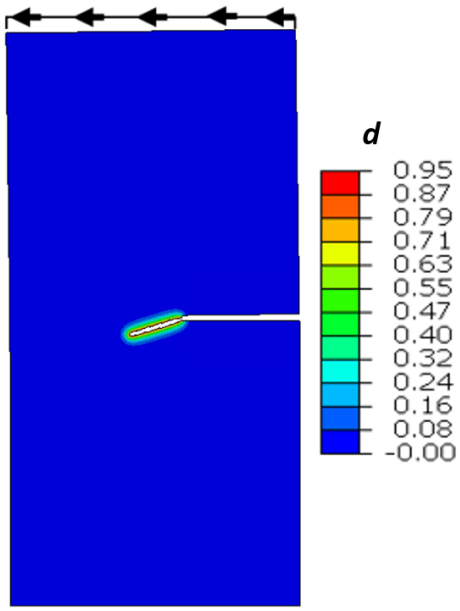

Figure 4.17: Damage in a cracked plate undergoing simple shear loading.

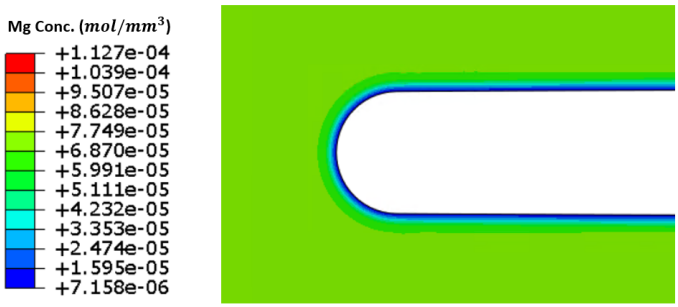

Figure 4.18: Concentration of Mg at crack tip after 24 hr of diffusion.

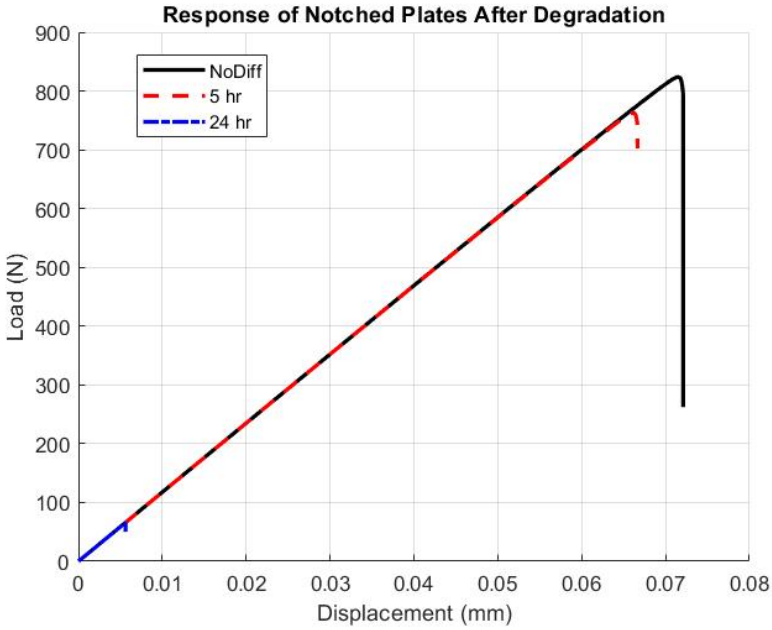

Figure 4.19: Load-displacement curves of the cracked plate before and after diffusion.

Chapter 5

Conclusion and Future Recommendations

5.1 Conclusion

In this work, a computational framework is developed to predict the constitutive response along with degradation and damage in magnesium implants subjected to stress-coupled chemically corrosive environment. For the elasto-plastic constitutive behavior of the Mg-implants, a phenomenological model is developed based on the large deformation J_2 plasticity theory with an isotropic hardening of the yield surface. The degradation is assumed to be a diffusion-driven process, where Mg ions

diffuse out of the implant into the surrounding fluid, resulting in degraded mechanical properties of the material. A phase-field fracture model is also developed, which predicts the initiation and growth of cracks in the implant based on a smeared area of damage – approximating a sharp crack. Mechanical tests were conducted using 99.9% purity Mg immersed in HBSS. Due to the variability in the test data, only two sets of exposure (5h and 24h) were considered for validations. In the proposed model, the critical fracture energy G_c, characteristic length scale l_c, and reference shear strain rate ν_0 were modified as a function of Mg ion concentration to predict the change in mechanical response of the tensile specimen. The current model is able to predict the change in response of a round tensile after 5 hr with reasonable accuracy, however for 24 hr it struggled to model the full extent of degradation. When the diffusion is applied to a cracked plate geometry, the model does a better job of predicting the severe degradation that is expected. This study shows that an experimentally validated computational framework is capable of predicting the implant's degradation behavior in a physiological environment and could be useful for patient specific implant's design.

5.2 Future Recommendations

While the proposed model is a good starting point, in the future it would be beneficial to implement a physically motivated framework incorporating grain structure

information and an improved reaction-diffusion model to simulate the chemical corrosion. These would allow for a much more accurate representation of how corrosion affects the implant, and it may be able to capture phenomena such as an oxide layer formation or corrosion attacks such as pitting. It would be particularly interesting to see if one could combine pitting corrosion with the phase-field fracture model, as the pits would likely serve as a site for the initiation of fracture. Incorporating factors such as ambient temperature, concentration of Mg ions in the surrounding and how those affect the corrosion rates are also going to be important for the future study.

On the experimental side, more extensive testing would be beneficial for developing future models. Since there was an observed variability in the rate of corrosion, it may be wise to target a finer and more uniform microstructure with better resistance to corrosion by using methods such as annealing or severe plastic deformation. There are also many promising Mg alloys for implants which could be used, although these alloys or the fine microstructure may require the addition of complexities into the model. Since *in vitro* tests are known to have higher rates of corrosion than *in vivo*, solutions that are less corrosive than HBSS such as Dulbecco's Modified Eagle Medium could also be considered for future experiments. Lastly, the conduction of hydrogen evolution experiments would be helpful for quantifying the corrosion rate.

References

[1] Saris, N.-E. L.; Mervaala, E.; Karppanen, H.; Khawaja, J. A.; Lewenstam, A. *Clinica chimica acta* **2000**, *294*(1-2), 1–26.

[2] Park, J. B.; Bronzino, J. D. **2002**.

[3] Staiger, M. P.; Pietak, A. M.; Huadmai, J.; Dias, G. *Biomaterials* **2006**, *27*(9), 1728–1734.

[4] Zhang, E.; Xu, L.; Yang, K. *Scripta Materialia* **2005**, *53*(5), 523–527.

[5] Davis, J. R. *Handbook of materials for medical devices;* ASM international, 2003.

[6] Revell, P. A.; Damien, E.; Zhang, X.; Evans, P.; Howlett, C. R. In *Key Engineering Materials*, Vol. 254, pages 447–450. Trans Tech Publ, 2004.

[7] Yoshizawa, S.; Brown, A.; Barchowsky, A.; Sfeir, C. *Acta biomaterialia* **2014**, *10*(6), 2834–2842.

[8] Yamasaki, Y.; Yoshida, Y.; Okazaki, M.; Shimazu, A.; Uchida, T.; Kubo, T.; Akagawa, Y.; Hamada, Y.; Takahashi, J.; Matsuura, N. *Journal of Biomedical Materials Research: An Official Journal of The Society for Biomaterials, The Japanese Society for Biomaterials, and The Australian Society for Biomaterials and the Korean Society for Biomaterials* **2002**, *62*(1), 99–105.

[9] Li, Z.; Gu, X.; Lou, S.; Zheng, Y. *Biomaterials* **2008**, *29*(10), 1329–1344.

[10] Winzer, N.; Atrens, A.; Dietzel, W.; Raja, V.; Song, G.; Kainer, K. *Materials Science and Engineering: A* **2008**, *488*(1), 339–351.

[11] Raja, V.; Padekar, B. S. *Corrosion Science* **2013**, *75*, 176–183.

[12] Choudhary, L.; Singh Raman, R.; Hofstetter, J.; Uggowitzer, P. J. *Materials Science and Engineering: C* **2014**, *42*, 629–636.

[13] Han, G.; Lee, J.-Y.; Kim, Y.-C.; Park, J. H.; Kim, D.-I.; Han, H.-S.; Yang, S.-J.; Seok, H.-K. *Corrosion Science* **2012**, *63*, 316–322.

[14] Song, G. *Corrosion Science* **2007**, *49*(4), 1696–1701.

[15] Shi, Z.; Hofstetter, J.; Cao, F.; Uggowitzer, P. J.; Dargusch, M. S.; Atrens, A. *Corrosion Science* **2015**, *93*, 330–335.

[16] Hofstetter, J.; Becker, M.; Martinelli, E.; Weinberg, A.; Mingler, B.; Kilian, H.; Pogatscher, S.; Uggowitzer, P.; Löffler, J. 04 **2014**.

[17] Song, D.; Ma, A.; Jiang, J.; Lin, P.; Yang, D.; Fan, J. *Corrosion Science* **2010**, *52*(2), 481–490.

[18] Zheng, T.; Hu, Y.; Yang, S. *Journal of Magnesium and Alloys* **2017**, *5*(4), 404–411.

[19] Liu, Y.; Liu, D.; You, C.; Chen, M. 09 **2015**, *9*.

[20] Ahmadkhaniha, D.; Järvenpää, A.; Jaskari, M.; Sohi, M. H.; Zarei-Hanzaki, A.; Fedel, M.; Deflorian, F.; Karjalainen, L. *Journal of the Mechanical Behavior of Biomedical Materials* **2016**, *61*, 360–370.

[21] Sanchez, A. H. M.; Luthringer, B. J.; Feyerabend, F.; Willumeit, R. *Acta Biomaterialia* **2015**, *13*, 16–31.

[22] Bowen, P.; Drelich, A.; Drelich, J.; Goldman, J. 01 **2015**, *103*.

[23] Bowen, P. K.; Drelich, J.; Goldman, J. *Materials Science and Engineering: C* **2013**, *33*(8), 5064–5070.

[24] Gastaldi, D.; Sassi, V.; Petrini, L.; Vedani, M.; Trasatti, S.; Migliavacca, F. 10 **2010**, *138*, 85–91.

[25] Ahmed, S. K.; Ward, J. P.; Liu, Y. *Materials* **2017**, *11*.

[26] Grogan, J.; Leen, S.; McHugh, P. *Acta Biomaterialia* **2014**, *10*(5), 2313–2322.

[27] Gartzke, A.-K.; Julmi, S.; Klose, C.; Waselau, A.-C.; Meyer-Lindenberg, A.; Maier, H. J.; Besdo, S.; Wriggers, P. *Journal of the mechanical behavior of biomedical materials* **2020**, *101*, 103411.

[28] Ambati, M.; Gerasimov, T.; De Lorenzis, L. *Computational Mechanics* **2015**, *55*(2), 383–405.

[29] Ambati, M.; Gerasimov, T.; De Lorenzis, L. *Computational mechanics* **2015**, *55*(5), 1017–1040.

[30] Miehe, C.; Hofacker, M.; Schänzel, L.-M.; Aldakheel, F. *Computer Methods in Applied Mechanics and Engineering* **2015**, *294*, 486–522.

[31] Borden, M. J.; Hughes, T. J.; Landis, C. M.; Anvari, A.; Lee, I. J. *Computer Methods in Applied Mechanics and Engineering* **2016**, *312*, 130–166.

[32] Bourdin, B.; Francfort, G. A.; Marigo, J.-J. *Journal of the Mechanics and Physics of Solids* **2000**, *48*(4), 797–826.

[33] Miehe, C.; Hofacker, M.; Welschinger, F. *Computer Methods in Applied Mechanics and Engineering* **2010**, *199*(45-48), 2765–2778.

[34] Gurtin, M. E. *Physica D: Nonlinear Phenomena* **1996**, *92*(3), 178–192.

[35] Stumpf, H.; Hackl, K. *International Journal of Solids and Structures* **2003**, *40*(6), 1567–1584.

[36] Wilson, Z. A.; Borden, M. J.; Landis, C. M. 10 **2013**, *183*(2), 135–153.

[37] Kumar, M.; Capolungo, L.; McCabe, R.; Tomé, C. 03 **2019**, *9*.

[38] Witte, F.; Kaese, V.; Haferkamp, H.; Switzer, E.; Meyer-Lindenberg, A.; Wirth, C.; Windhagen, H. *Biomaterials* **2005**, *26*(17), 3557–3563.

[39] Witte, F.; Hort, N.; Vogt, C.; Cohen, S.; Kainer, K. U.; Willumeit, R.; Feyerabend, F. *Current opinion in solid state and materials science* **2008**, *12*(5-6), 63–72.

[40] Witte, F.; Fischer, J.; Nellesen, J.; Crostack, H.-A.; Kaese, V.; Pisch, A.; Beckmann, F.; Windhagen, H. *Biomaterials* **2006**, *27*(7), 1013–1018.

[41] Song, G. *Corrosion science* **2007**, *49*(4), 1696–1701.

[42] Gu, X.; Zheng, Y.; Cheng, Y.; Zhong, S.; Xi, T. *Biomaterials* **2009**, *30*(4), 484–498.

[43] Francfort, G. A.; Marigo, J.-J. *Journal of the Mechanics and Physics of Solids* **1998**, *46*(8), 1319–1342.

[44] Miehe, C.; Schaenzel, L.-M.; Ulmer, H. *Computer Methods in Applied Mechanics and Engineering* **2015**, *294*, 449–485.

[45] Konica, S.; Sain, T. *Journal of the Mechanics and Physics of Solids* **2021**, *150*, 104347.

[46] *Int. J. Miner. Metall. Mater. 22*.

[47] Francfort, G.; Marigo, J.-J. *Journal of the Mechanics and Physics of Solids* **1998**, *46*(8), 1319–1342.